Mixed Electronic-Ionic Conductivity of Cobalt Doped Cerium Gadolinium Oxide

C.M. KLEINLOGEL & L.J. GAUCKLER*

*ETH-Zürich, Swiss Federal Institute of Technology, Department of Materials, Nonmetallic Materials, CH-8092 Zurich, Switzerland,
fax: +41 1 632 11 32 E-mail: kleinlogel@nonmet.mat.ethz.ch*

Abstract. The effect of small amounts ($< 5\,\mathrm{mol}\,\%$) of cobalt oxide on the electrical properties of cerium oxide solid solutions has been evaluated. $Ce_{0.8}Gd_{0.2}O_{2-x}$ (CGO) powder with an average crystallite size of 20 nm served as a model substance for the electrolyte material with a high oxygen ion conductivity and low electronic conductivity in its densified state. Doping the CGO powder by transition metal oxides (MeO) with concentrations below $2\,\mathrm{mol}\,\%$ did not change the ionic conductivity nor the electrolytic domain boundary. After long sintering times (2 h) at temperatures above $900°C$, MeO and CeO_2 form solid solutions. However, short sintering times or high dopant concentrations lead to an electronic conducting grain boundary phase short circuiting the ionic conductivity of the CGO grains. Choosing proper doping levels, sintering time and temperature allows one to tailor mixed conducting oxides based on CGO. These materials have potential use as electrolytes and/or anodes in solid oxide fuel cells and ion separation membranes.

Keywords: ceria solid solutions, mixed ionic electronic conductivity, nanosized ceramic, transition metal oxides, cobalt oxide, brick layer model

1. Introduction

1.1. General

Solid electrolytes exhibiting high oxygen ion conductivity are of special interest for their application in electrochemical devices such as solid oxide fuel cells (SOFCs), oxygen separation membranes and methane gas conversion reactors. In the case of SOFCs, the state-of-the-art material is yttria stabilized zirconia which exhibits sufficient ionic conductivity at an operating temperature of $900°C$ to $1000°C$ [1]. This high temperature requires expensive materials for interconnectors, heat exchangers, and structural components. It is therefore desirable to lower the operating temperature to intermediate temperatures of about $700°C$. This requires either new system concepts such as thin-film electrolyte SOFCs [2,3,4] or new electrolyte materials with higher oxygen ion

conductivity [5,6,7]. Ceria solid solutions have been shown to exhibit 4 to 5 times higher ionic conductivities at intermediate temperatures [8] compared to zirconia. Although ceria based electrolytes are slightly reduced at low oxygen partial pressures and thereby develop increasingly higher electronic conductivity [9], it has been shown that CGO based SOFCs can be operated at temperatures as low as $700°C$ with high power output and high efficiency [10,11]. Therefore, CeO_2-based solid solutions (CeO_2ss) are attractive electrolytes in SOFCs. In a recent paper [12] it was also shown that CeO_2 containing anodes exhibit catalytic activity that allow SOFCs to operate below $700°C$ with natural gas without carbon deposition.

One problem arising from ceria-based electrolytes for SOFCs is that conventional sintering to full density requires temperatures exceeding $1300°C$ [13–18]. As consequence, high grain growth rates and large grains of several μm were observed resulting in poor mechanical stability of the ceramic

* Corresponding author.

component. This characteristic is one of the major reasons which hinders the use of CeO_2ss in SOFC applications despite their superior electrochemical performance.

1.2. Aim of the Study

In our previous work we have shown that sintering of cerium oxide solid solutions with initial grain sizes in the nanometer range is strongly promoted when adding small amounts ($\sim 1 \, mol \%$) of transition metal oxides (e.g., cobalt oxide) [19,20]. We succeeded in obtaining $>99\%$ dense electrolytes with grain sizes of $\sim 120 \, nm$ after sintering at temperatures as low as 900°C. It was also observed that when interrupting sintering of a cobalt oxide doped cerium oxide sample, an approximately 2 nm thick amorphous cobalt rich grain-boundary layer was present. This layer disappears after thermally equilibrating the dense sample for longer sintering times or when higher sintering temperatures are used.

Now the question arises whether these nanosized cerium oxide based ceramics, sintered at relatively low temperatures, still exhibit electrochemical properties suitable for use as electrolytes or electrodes in intermediate temperature solid oxide fuel cells. Of particular interest is the influence of cobalt incorporated within the ceria lattice on the mixed ionic/electronic conductivity as well as the properties of CGO with cobalt oxide rich grain-boundary films. We want to investigate the formation as well as the dissolution of the cobalt rich grain-boundary layer and its effect on the grain/grain-boundary conductivity. The sample composition and also the sintering program have been varied in order to show the relation between the microstructures and the electrochemical behavior.

2. Experimental Procedures

2.1. Sample Preparation

$Ce_{0.8}Gd_{0.2}O_{2-x}$ (denoted CGO; #595250A, Rhodia GmbH, Frankfurt, FRG) with a crystallite size of 20 nm and a specific surface area of about $24 \, m^2/g$ was used as starting powder to which the dopant was added in form of the nitrate ($Co(NO_3)_2 \cdot 6H_2O$, Fluka AG, Buchs, CH). Doping of CGO with different concentrations of cobalt oxide (0–5 mol %) was

performed by first dispersing the CGO powder in ethanol (Fluka, puriss.p.a.), using an agate mortar. A desired amount of the dissolved dopant nitrate was then added. After drying at 120°C for two hours the powders were first uniaxially dry pressed at 50 MPa into pellets with a diameter of 10 mm followed by isostatic pressing at 840 MPa for 3 min.

Sintering of the pressed pellets has been conducted in air on magnesium oxide plates. The heating rate was fixed to 1 K/min up to 400°C followed by 3 K/min up to the desired temperature. After annealing at the sintering temperature, the samples were cooled at 5 K/min to room temperature. The final densities of the sintered pellets, determined following the Archimedes method, have been $>98\%$ of the throretical density.

2.2. Impedance Spectroscopy and 4-Point Conductivity Measurements

Both sides of a polished sample pellet were contacted by first sputtering a $\sim 50 \, nm$ Pt layer (model SCD 040, Baltec, Balzers, FL) followed by fixing platinum wires (0.35 mm diameter) with a ceramic two-component binder (type 1500, Friag, Ebmatingen, CH) and finally coating with platinum paste (C 3605 P, Hereaus GmbH, Hanau, FRG). The electrodes were then heat treated at 700°C for two hours to burn out the binder of the platinum paste and to ensure good contact of the electrodes with the ceramic pellet. AC impedance spectroscopy was performed on each of the pellets in a temperature range from 150°C to 700°C using a Zahner FRA (model IM6, Zahner GmbH, Kranach, FRG) in the range 0.1 Hz–2 MHz with an excitation voltage of 50 mV at $T < 400°C$ and 10 mV at temperatures above. The measurements were carried out in air and in different gas mixtures (N_2, CO/CO_2, N_2/H_2) over a P_{O_2} range from 0.21 to 10^{-27} atm. The P_{O_2} value was recorded using a zirconia based probe located close to the sample.

4-point conductivity measurements were carried out on test bars of $30 \cdot 4 \cdot 4 \, mm$ (length $\cdot$ width $\cdot$ height) contacted by applying platinum paste and fixing platinum wires with a ceramic two-component binder. Measurements were taken in air during heating up to 900°C as well as during annealing and cooling to room temperature to confirm reproducibility.

2.3   Microstructural Modeling

In order to correlate the measured electrical properties with the sample microstructure the so called ''brick layer model'', hereafter referred to as BLM, has been applied. The BLM was first proposed by Beekmans and Heyne [21] and further refined by Dijk and Burgraaf [22]. Their models are based on the work of Bauerle [23] who first developed an equivalent circuit model for conductive ceramics with resistive grain boundaries. Most recently, Hwang et al. [24] applied the BLM to nanocrystalline CeO_2 with enhanced conduction at grain boundaries discussing the limitations of this model for complex electroceramic microstructures. A general representation of the BLM is shown in Fig. 1. The grains are modeled as cubes of equal size and edge length, D, surrounded by a grain boundary of a specific thickness, δ_{gb}. For the apparent grain size it follows then: $\langle D \rangle = D + \delta_{gb}$. The current flow is assumed to be one-dimensional, and the curvature of the current paths at the corners of the grains is neglected. Depending on the relative magnitudes of the grain and grain boundary conductivities σ_{gr} and σ_{gb}, the current largely flows either through grains and across grain-boundaries (Fig. 2, path 1) or along grain-boundaries (Fig. 2, path 2).

Case I: $\sigma_{gb} \ll \sigma_{gr}$ *and* $\delta_{gb} \ll \langle D \rangle$. If the grain boundary conductivity, σ_{gb}, is much smaller than the conductivity of the grain interior, σ_{gr}, and/or the grain boundary thickness is small compared to the grain size $(\delta \ll \langle D \rangle)$, then only contributions from grain boundaries perpendicular to the electric flux have to

Fig. 2. Equivalent circuit representation of microstructures according the BLM. Two current paths are possible. Path 1: perpendicular crossing of grain and grain-boundary. Path 2: Short circuiting grains, current flows along parallel grain-boundaries. R_1 represents the ohmic contribution of current leads and contacts; R_2 and C_2 represent the electrode response.

be considered. Contributions from grain boundaries parallel to the electric flux, i.e., short-circuiting the grain contribution, can be neglected. This situation results in a Bauerle-type equivalent circuit consisting of two parallel RC (resistor-capacitor) elements in series representing the grain and grain-boundary contribution, respectively (Fig. 2, path 1).

From impedance spectra in which the imaginary part Im(Z) is plotted against the real part Re(Z) of the impedance, the grain resistance, R_{gr}, and the total grain-boundary resistance, R_{gb}, can be obtained from the intersections on the real axis of the corresponding semicircular arcs (Fig. 3). As the frequency peak of each semicircle is given by
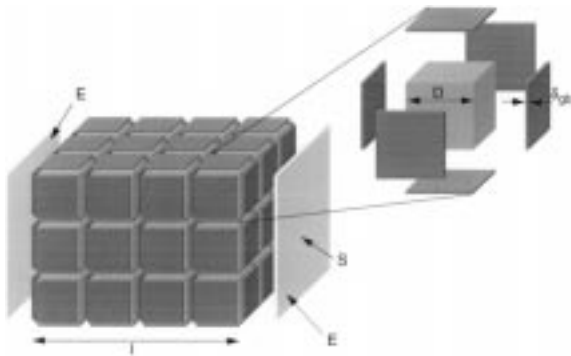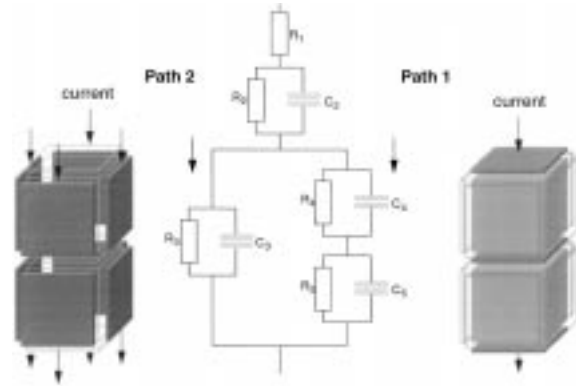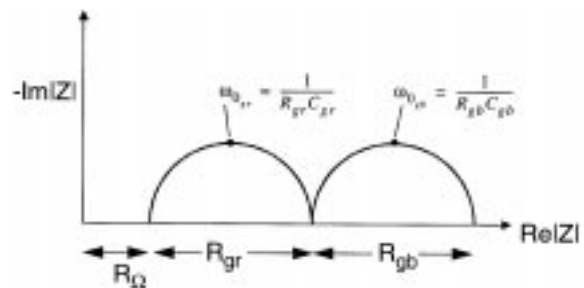
$$\omega_{0_i} = \frac{1}{R_i C_i} \tag{1}$$

Fig. 1. Sketch of the brick-layer-model, BLM, indicating grain diameter, D, grain-boundary thickness, δ_{gb}, sample thickness, l, cross-sectional area, S and electrodes, E.

Fig. 3. Sketch of a Nyquist plot representing path 1 of Fig. 2. Grain and grain-boundary arcs are separated.

the specific capacitances, C_i, can be calculated. We also know that C_i is defined as $C_i = \varepsilon_0 \varepsilon_r\, S/l$ and using $\sigma_i = l/(SR_i)$ it follows that

$$\frac{1}{\omega_{0_i}} = R_i C_i = \frac{1}{\sigma_i}\varepsilon_i \varepsilon_0 \qquad (2)$$

where ε_i denotes the specific relative dielectric constant, and ε_0 the permittivity of free space. S corresponds to the electrode area and l to the thickness of the sample. It is important to note that ω_{0_i} is an intrinsic material property, independent of geometric considerations. Since the dielectric constant in sintered materials does not vary significantly on a spacial basis compared to the conductivity, it is reasonable to make the usual assumption that $\varepsilon_{gr} \approx \varepsilon_{gb}$ [25,26]. This holds also for cobalt doped cerium oxide since ε_r for cerium oxide is about 30 and for cobalt oxide about 40 [27,28]. However, the conductivity may easily change orders of magnitude as we will show later. Therefore, distinct arcs for grain and grain-boundary contributions in an impedance spectra (c.f. Fig. 3) can only be observed if $|\sigma_{gr} - \sigma_{gb}| \gg 0$, which is true for the present case.

It follows that the capacitance ratio of the two components is:

$$\frac{C_{gb}}{C_{gr}} = \frac{\varepsilon_{gb}}{\varepsilon_{gr}} \cdot \frac{\langle D \rangle}{\delta_{gb}} \qquad (3)$$

The total bulk capacitance, C_{gr}, and the effective total grain-boundary capacitance, C_{gb}^T, are given by

$$C_{gr} = \frac{\varepsilon_{gr}\varepsilon_0 \cdot S}{l} \qquad (4)$$

$$C_{gb}^T = \frac{\varepsilon_{gb}\varepsilon_0 \cdot S}{l} \qquad (5)$$

ε_{gr} is the bulk relative dielectric constant and ε_{gb} the grain-boundary relative dielectric constant. Equation (3) establishes a connection between microstructure and electrical properties allowing to relate the microscopically observed grain-boundary thickness estimated from electrical properties.

Furthermore, the grain conductivity, σ_{gr}, and the effective total grain-boundary conductivity, σ_{gb}^T, are given by:

$$\sigma_{gr} = \frac{1}{R_{gr}}\frac{l}{S} \qquad (6)$$

$$\sigma_{gb}^T = \frac{1}{R_{gb}}\frac{l}{S} \qquad (7)$$

and we can then define the specific grain-boundary conductivities as

$$\sigma_{gb}^{sp} = \frac{\sigma_{gb}^T \delta_{gr}}{\langle D \rangle} \qquad (8)$$

The interpretation of the impedance spectra in the case discussed above is straightforward. In a two arc spectrum (c.f. Fig. 3) (we do not consider electrode effects here) one can interpret the highest frequency arc representing the bulk response followed by the grain-boundary signal at lower frequency.

It is important to note that for impedance spectra which exhibit two clearly separated arcs, one can immediately deduce that $\sigma_{gb} < \sigma_{gr}$ since only a difference in conductivities of grain and grain-boundary can give a difference in characteristic frequencies.

Case II: $\sigma_{gb} \gg \sigma_{gr}$ and $\delta_{gb} \ll \langle D \rangle$. In this particular case the grain-boundary width is small compared to the apparent grain-size $\langle D \rangle$, but the grain-boundary conductivity, σ_{gb}, is much higher than the grain conductivity, σ_{gr}. Therefore the current flows mainly along grain boundaries, i.e., short circuiting the grain current, and the above discussed BLM is then reduced to one single RC circuit (c.f. Fig. 2, path 2). A ceramic sample will then show only one arc in the impedance plot (Fig. 4) and little information will be gained about the microstructure. However, if some micro-
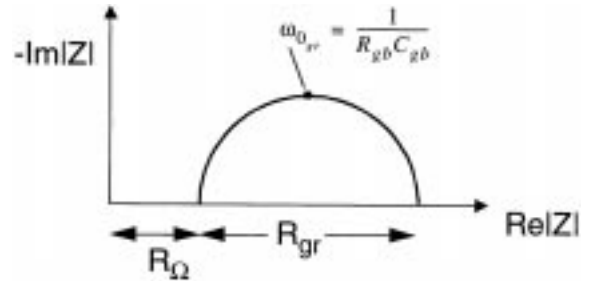

Fig. 4. Sketch of a Nyquist plot representing path 2 of Fig. 2. Only one arc can be observed here representing a highly conductive grain-boundary phase.

structural data are available such as grain-boundary thickness, σ_{gb} may be estimated and some information about the composition of the grain-boundary and its specific properties can be deduced.

Previously reported applications of the BLM on single-crystalline and polycrystalline materials. Using impedance spectra alone allows one to distinguish between conducting grains with blocking grain boundaries on the one hand and poorly conducting grains with highly conducting grain-boundaries on the other. Other groups have extensively used the BLM on doped and undoped cerium oxide single crystals as well as on polycrystalline cerium oxide. Christie et al. [27] applied the BLM to $Ce_{0.8}Gd_{0.2}O_{2-x}$ with micrometer and sub-micrometer sized grains. They found the grain-boundary conductivity to be strongly dependent on the microstructure. Gödickemeier et al. [29] applied the BLM on 3Y-TZP containing small amounts of SiO_2 and Al_2O_3. Characteristics of the intergranular glass film in terms of equilibrium thickness and microscopic permittivity, were determined from the impedance plots.

The limitation of the BLM has been discussed by several authors. Näfe [30] combined the two extremes described in Fig. 2 in one expression, and showed the validity of the BLM analyzing the conductive behavior of different materials.

2.4. Defect Chemistry of Gadolinium Doped Cerium Oxide Containing Ions of Variable Charges

Introduction of electronic conductivity in solid electrolytes by heavy doping with transition metal or rare earth ions has been widely discussed in terms of e.g., enlarging the triple phase boundary at electrode/electrolyte interfaces [31,32], enhancement of the oxygen exchange coefficient at the electrolyte surface [33], increasing the oxygen exchange coefficient and the electrocatalytic activity at electrolyte surfaces [34–36]. For doping of yttria stabilized zirconia single crystals with transition metals and rare earth ions of variable charges, Sasaki showed that the equilibrium concentrations of electrons and holes are not effected as long as the dopant level of the redox active species is kept low and equilibrium conditions are present [37].

In the following, we will show that low level ($\sim 1\,mol\,\%$) doping of cerium gadolinium oxide with transition metal oxides such as cobalt oxide does not

significantly effect the overall conductivity of the bulk material. First, we will consider conditions in temperature and P_{O_2} where ceria based solid electrolytes exhibit an ionic transference number close to unity, i.e., they are mainly oxygen ion conducting. Secondly, we will use operating regimes where Ce^{4+} becomes partially reduced to Ce^{3+} thus showing an increase in σ_e and consequently exhibiting an ionic transference number less than one.

Defect chemistry of cerium gadolinium oxide assuming no partial reduction of cerium. The defect chemistry, described in Kröger-Vink notation, is considered only for situations where $[V_O^{\bullet\bullet}] \gg [h^\bullet], [e']$ and $[V_O^{\bullet\bullet}] \gg [M] \cdot c_M \equiv [M]$ denotes the concentration of dopant with variable charges.

The equilibrium defect chemistry at a temperature, T, and an oxygen partial pressure, P_{O_2}, is described by the oxygen incorporation equilibrium:

$$V_O^{\bullet\bullet} + (1/2)O_2 \leftrightarrow O_O^x + 2h^\bullet \tag{9}$$
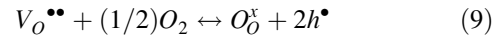
giving the mass action constant K_1 as:

$$K_1(T,\,P_{O_2}) = \frac{[h^\bullet]^2 \cdot [O_0^x]}{[V_O^{\bullet\bullet}] \cdot P_{O_2}^{1/2}} \tag{10}$$

Herein $[O_O^x]$ can be assumed as constant.

Since $[V_O^{\bullet\bullet}] \gg [h^\bullet], [e'], [M'_{Ce}], [M''_{Ce}]$ the overall electroneutrality condition

$$2[V_O^{\bullet\bullet}] + [h^\bullet] - [Gd'_{Ce}] - [e'] - [M'_{Ce}] - 2[M''_{Ce}] = 0 \tag{11}$$

is then reduced to:

$$2[V_O^{\bullet\bullet}] \cong [Gd'_{Ce}] \tag{12}$$
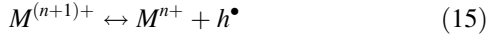
From this, we can deduce the electron and the hole concentration which are fixed by T, P_{O_2}, $[Gd'_{Ce}]$ and K_1, K_2 respectively, where K_2 is the electron-hole equilibrium and given by $[e'] \cdot [h^\bullet] = K_2(T, P_{O_2})$:

$$[h^*] = K_1^{1/2}[V_O^{\bullet\bullet}]^{1/2} \cdot P_{O_2}^{1/4} \cong K_1^{1/2} \cdot \left(\frac{[Gd'_{Ce}]}{2}\right)^{1/2} \cdot P_{O_2}^{1/4} \tag{13}$$

and

$$[e'] = K_2/[h^*] \cong K_1^{-1/2} \cdot K_2 \cdot \left(\frac{[Gd'_{Ce}]}{2}\right)^{-1/2} \cdot P_{O_2}^{-1/4} \tag{14}$$

Impurity equilibria such as:

$$M^{(n+1)+} \leftrightarrow M^{n+} + h^\bullet \qquad (15)$$

with an equilibrium constant K_3 given by

$$K_3(T, P_{O_2}) \equiv \frac{[M^{n+}] \cdot [h^\bullet]}{[M^{(n+1)+}]} \qquad (16)$$

are not of influence on $[h^\bullet]$, $[e']$, rather the ratio of $[M^{n+}]/[M^{(n+1)+}]$ is fixed through Eq. (13) and Eq. (16). This means that the electron and hole concentrations in cerium oxide are not affected by the redox-active species, as long as the simplification of the overall electroneutrality condition (Eq. (12)) is valid. Using the mass conservation condition,

$$c_M = [M^{(n+1)+}] + [M^{n+}] \qquad (17)$$

the concentrations $[M^{n+}]$ and $[M^{(n+1)+}]$ can be easily calculated. It follows for low P_{O_2}):

$$[M^{n+}] \cong c_M \quad \text{and} \quad [M^{(n+1)+}] \cong c_M \cdot K_1^{1/2} K_3^{-1}$$

$$\cdot \left(\frac{[Gd'_{Ce}]}{2} \right)^{1/2} \cdot P_{O_2}^{1/4} \qquad (18)$$

and for high P_{O_2}

$$[M^{(n+1)+}] \cong c_M \quad \text{and} \quad [M^{n+}] \cong c_M \cdot K_1^{-1/2} K_3$$

$$\cdot \left(\frac{[Gd'_{Ce}]}{2} \right)^{-1/2} \cdot P_{O_2}^{-1/4} \qquad (19)$$

These defect chemistry relations are, of course, different if the total M-concentration, c_M, becomes comparable with $[Gd'_{Ce}]$ (Eq. (12) invalid). Moreover, at much higher M-concentrations, the hopping electron conduction between $[M^{n+}]$ and $[M^{(n+1)+}]$ may not be negligible [38]. However, as in our study we are dealing with transition metal oxide concentrations as low as ~ 1 cat % compared to 20 cat % of gadolinium incorporated in cerium oxide, this effect does not need to be considered.

Defect chemistry of cerium gadolinium oxide taking into account partial reduction of cerium oxide. Ceria and ceria solid solutions are reduced and become nonstoichiometric under low oxygen partial pressures, e.g., on the anode side of solid oxide fuel cells (SOFC). The reduction of ceria introduces free electrons responsible for mixed ionic electronic conductivity [9,39,40,41]. The oxygen content in nonstoichiometric ceria is then changed by the electrochemical reaction

$$2Ce_{Ce}^x + O_O^x \leftrightarrow 2Ce'_{Ce} + V_O^{\bullet\bullet} + \frac{1}{2}O_2 \qquad (20)$$
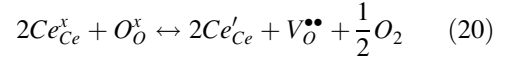
giving:

$$K_4(T) = \frac{[Ce'_{Ce}]^2 \cdot [V_O^{\bullet\bullet}] \cdot P_{O_2}^{1/2}}{[Ce_{Ce}^x]^2 \cdot [O_O^x]} \qquad (21)$$

Herein $[Ce_{Ce}^x]$, $[O_O^x]$ and $[V_O^{\bullet\bullet}]$ can be assumed as constant. Since $[e'] = [Ce'_{Ce}]$ an n-type electronic conductivity giving a slope of -0.25 in a $\log(\sigma)$ versus $\log(P_{O_2})$ plot can be found [38,42].

3. Results

3.1. Total Conductivity

To investigate the influence of CoO dopant on the oxygen ionic conductivity, σ_i, of CGO we first performed 4-point measurements measurements to determine the total electrical conductivity σ_{tot} (the sum of σ_i and the electronic conductivity σ_e). The activation energy, E_A, was then derived from the slope in the $\ln(\sigma_{tot}T)$ versus $1/T$ plot. Furthermore, we carried out conductivity measurements in different gas atmospheres and at different temperatures to find the electrolytic domain boundary, i.e., where σ_i equals σ_e.

The total conductivity, σ_{tot}, of CGO as a function of CoO concentration at 600°C, 700°C, and 800°C in air is plotted in Fig. 5. The sintering temperatures (two hours annealing time each) were as follows: 1400°C for pure, 0.01 and 0.1 mol % doped, 1100°C for 0.5 mol %, and 1000°C for > 1 mol % of cobalt oxide.
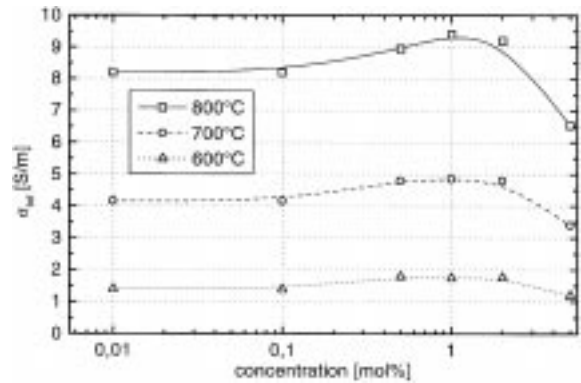

Fig. 5. Total conductivity, σ_{tot}, for $Ce_{0.8}Gd_{0.2}O_{2-x}$ doped with different concentrations of CoO at 600, 700 and 800°C in air (sintered at 1000°C for 2 h).

We found that the conductivity σ_{tot} remains unchanged for concentrations ranging from 0 to 2 mol % compared to pure CGO. Exceeding 2 mol % of dopant a somewhat lower σ_{tot} was noticed.

Sintering of 5 mol % CoO doped CGO sample at 1000°C for two hours does not lead to a fully equilibrated sample. This can be seen from Fig. 6 where $\log(\sigma_{tot})$ is plotted versus 1/T for CGO samples with dopant concentrations of 0.5, 2 and 5 mol %. The conductivity shown was recorded during heating and cooling. We found a hysteresis at temperatures below 400°C indicating a higher conductivity for the as-sintered sample. After a second cycle up to 900°C the conductivity was similar to pure and < 5 mol % doped samples. This suggests that a highly conducting phase is present which increases the total conductivity about one order of magnitude at 250°C. This phase vanishes after two heating cycles as well as with increasing sintering time or increasing sintering temperature resulting in σ_{tot} comparable to pure CGO. In the following subsection (3.2) we will further analyse this behavior in terms of grain/grain-boundary conductivity contributions.

Figure 7 shows a comparison of the total electrical conductivities in air determined by impedance spectroscopy and by 4-point measurements for 1 mol % CoO doped samples sintered at 1000°C for two hours. We also plotted results reported earlier [43] determined by 4-point measurements. The actual measurements are in very good agreement with our
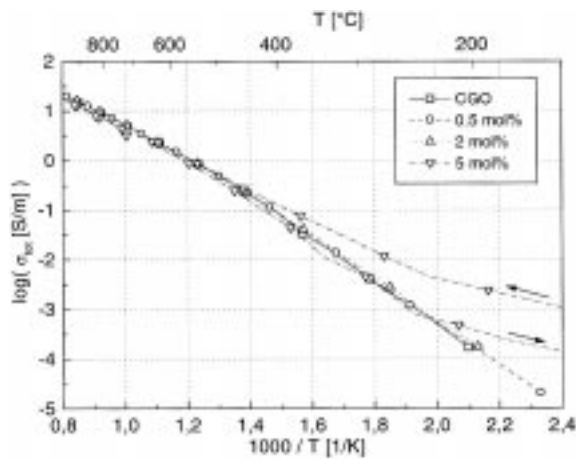

Fig. 7. Arrhenius plot of the total conductivity, σ_{tot}, of CGO doped with 1 mol % CoO determined with 4-point and impedance spectroscopy. For comparison the results of Gödickemeier [43] are added.

previous ones, only at temperatures above 700°C slightly higher values were obtained for the present samples.

Since the total conductivity $\sigma_{tot} = \sigma_i + \sigma_e$, it may be argued that there is a contribution to σ_{tot} via a percolating semi conducting cobalt oxide grain boundary layer (σ_e) which equals the loss in σ_i. This contribution seems to be evident for the 5 mol % and 2 h sintered sample (c.f. Fig. 6) but perhaps it is also present in the samples containing lower dopant concentrations.

To elucidate this point, we conducted further measurements on the P_{O_2} dependence of the total conductivity, σ_{tot}. In Fig. 8, σ_{tot} for CGO doped with 1 mol % CoO ($T_s = 1000$°C for two hours) is plotted as a function of P_{O_2} ranging from 0.21 to 10^{-27} atm. We found at high P_{O_2} the conductivity is predominantly ionic and at lower P_{O_2} the material becomes a mixed ionic/electronic conductor due to partial reduction of Ce^{4+} to Ce^{3+} (c.f. Eqn. (20)). The solid lines are fits to $\sigma_e \sim P_{O_2}^{-1/m}$ where 1/m was fixed to 0.25, which means that the number of oxygen vacancies can be assumed as constant (c.f. subsection 2.4). Activation energies E_A obtained from the $\ln(\sigma_{tot}T)$ versus 1/T plot in air (c.f. Fig. 7) as well as data for the ionic conductivity (σ_i) and the electrolytic domain boundary (EDB) are listed in Table 1. These results compare well with our former results and with literature data.

We can further calculate from the formation

Fig. 6. Total conductivity, σ_{tot}, of CGO doped with CoO (0, 0.5, 2, 5 mol %) after sintering at 1000°C for 2 h. The arrows indicate the heating and cooling cycle of the 5 mol % sample.
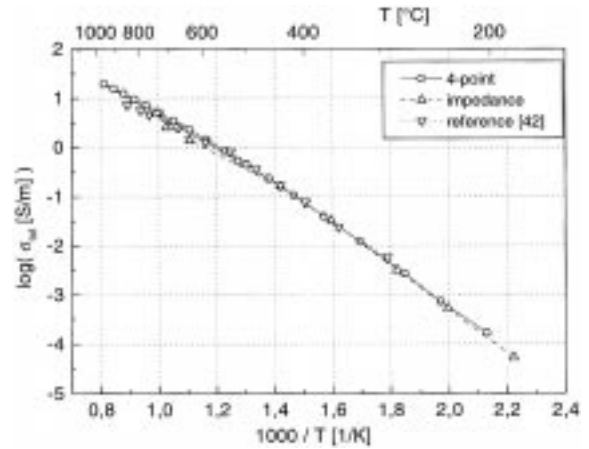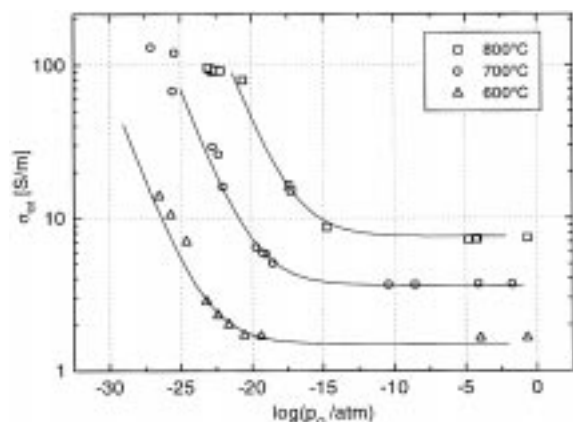
Fig. 8. Total conductivity of $Ce_{0.8}Gd_{0.2}O_{2-x}$ doped with 1 mol% CoO as a function of P_{O_2} at different temperatures. The sample was sintered at 1000°C for 2 h.

enthalpy of cobalt oxide [44] that e.g., at 700°C it will be reduced to metallic cobalt at a P_{O_2} below 10^{-22} atm. This is much higher than the P_{O_2} reached during the measurement which was about $\sim 10^{-26}$ atm. We have not, however, found an increase in σ_e which can be attributed to a percolating cobalt metal grain boundary layer.

From these results we deduce that there is no cobalt oxide rich grain boundary layer formed which may block oxygen ions in samples of doping levels below 5 mol% after sintering at 900°C for dwell times ≥ 2 h or at temperatures ≥ 1000°C. At higher doping levels (~ 5 mol%) we found a strong indication of a cobalt oxide rich phase forming a percolating network thus increasing the electronic conductivity. However, this electron conducting layer vanishes after further heat treatment implying the dissolution of the cobalt cations within the ceria lattice.

This experimental result is consistent with the model described above (subsection 2.4) where we showed that doping of CGO with multivalent transition metal will not introduce electronic conductivity by electrons or holes as long as the dopant level is kept low compared to the gadolinium concentration.

In the following subsection we will further analyse the conductivity behavior of a cobalt rich grain boundary in CGO. With impedance spectroscopy the grain and grain-boundary contributions to the overall conductivity have been separated and their evolution with sintering time was recorded.

3.2. Impedance Analysis of Grain/Grain-Boundary Contribution to Total Conductivity

To further analyze the conductivity behavior of the cobalt rich grain boundary layer in doped CGO we used impedance spectroscopy on 1 mol% CoO doped CGO sintered at 900°C with dwell times of 10 min, 2 and 50 h. Nyquist and Bode plots are shown in Fig. 9 and Fig. 10, respectively. We found that the 10 min sintered sample exhibits what appears to be a single arc which is centered on the real axis (Fig. 9(a)) giving a single plateau behavior in the bode plot (Fig. 10(a)). However, a slight distortion of the ideal "one relaxation time process" behavior indicates that there might be a second process present which could not be resolved due to a similar characteristic relaxation frequency, ω_0.

In contrast, samples sintered with 2 h dwell time exhibited two overlapping arcs (Fig. 9(b)) leading to a dual plateau behavior in the Bode plot (Fig. 10(b)). This indicates that a change in conductivity, i.e., a second conductivity mechanism contributes significantly to the overall impedance. Further increasing the dwell time up to 50 h gives two clearly separated high frequency arcs and an additional distinct third arc (marked C) at low frequency (Fig. 9(c) and Fig. 10(c)). From the model discussed in subsection 2.3 it

Table 1. Ionic conductivity, σ_i, electrolytic domain boundary, EDB, and activation energy for ionic conductivity, E_A, for doped and undoped CGO. For comparison literature data are given

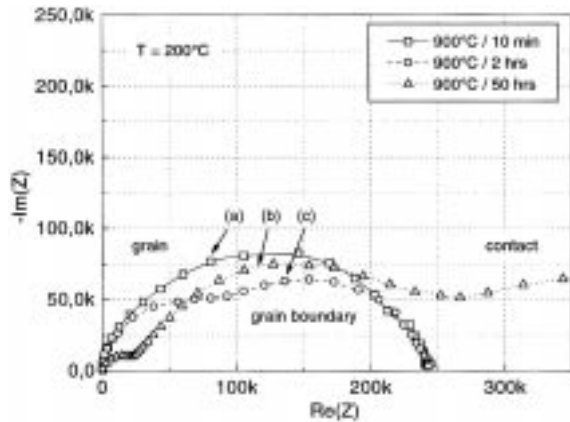| Material	σ_i [S/m] at 700°C	EDB [atm P_{O_2}] at 700°C	E_A[eV]
CGO	4.5	$1.78 \cdot 10^{-19}$	0.73
CGO + 1 mol% CoO	4.8	$2.2 \cdot 10^{-19}$	0.73
$Ce_{0.8}Gd_{0.2}O_{1.9-x}$ [9]	3.62	$1.14 \cdot 10^{-20}$	0.73
$Ce_{0.8}Gd_{0.2}O_{1.9-x}$ [45,46]	4.7	$1.24 \cdot 10^{-19}$	0.75
$Ce_{0.8}Gd_{0.2}O_{1.9-x}$ [47]	2.8	$3.5 \cdot 10^{-19}$	—

Fig. 9. Complex plane plot of the electrochemical response for different CoO doped $Ce_{0.8}Gd_{0.2}O_{2-x}$ samples sintered at 900°C with varying dwell times (10 min, 2 and 50 h). The results were obtained at 200°C in air. Plots have been normalized to the data of the specimen sintered at 900°C/10 min and corrected for ohmic contributions to illustrate the change in grain, grain boundary and contact contributions. Frequency increases from right to left.
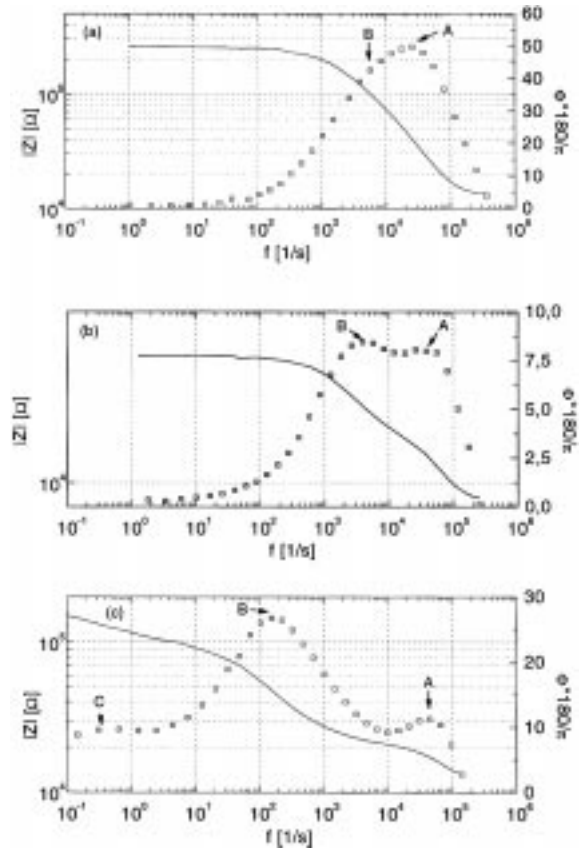

Fig. 10. Bode plot of 1 mol % CoO doped $Ce_{0.8}Gd_{0.2}O_{2-x}$ sintered at 900°C with varying dwell times (10 min (a), 2 h (b) and 50 h (c)). The spectra were recorded at 200°C. $|Z|$ is indicated by lines; phase angle ϕ, by open symbols.

becomes evident that the arcs A, B, and C are representing the grain, grain-boundary and electrode contribution to the total impedance. We can further note that ω_0 of the rising second arc (marked B in Fig. 10) shifts continuously to lower frequencies with increasing dwell time. This clearly indicates that the conductivity of the corresponding process decreases (c.f. Eq. (2)). In contrast, the characteristic frequency of the first arc (marked A in Fig. 10) remains constant with increasing dwell time implying a constant conductivity.

To investigate the temperature dependence of the conductivity of the samples we recorded the impedance at 150, 200, and 250°C (Figs. 11–13). The spectra reflect the temperature dependence of σ_{gr} and σ_{gb}, i.e., an increase of σ with increasing temperature. It is clear that the characteristic frequencies, ω_0, are shifting to higher frequencies (arrows in Fig. 11–13). From spectra recorded at higher temperatures ($>250°C$) the grain/grain-boundary contribution could not be clearly resolved any more and only the total contribution of both processes has been recorded.

Figure 14 shows an Arrhenius plot of the conductivity values obtained from the impedance spectra. The grain-boundary conductivity, σ_{gb}, is shown in the temperature range from 150 to about 400°C and the total conductivity, σ_{tot}, above 400 up to 700°C. Sintering at 900°C for 10 min leads to an

increase of σ_{gb} as well as to a decrease in activation energy, E_A, from about 0.81 to 0.54 eV compared to pure CGO. With dwell times longer than 2 h a higher σ_{gb} with $E_A = 0.54$ eV was still observed. However the temperature where the slope changes to higher E_A which means when σ_{gr} equals σ_{gb} shifts from about 400°C to 300°C. Further increase of dwell time up to 50 h leads to σ_{tot} and E_A comparable to pure CGO.

A similar influence on conductivity has been found for 5 mol % doped samples as shown in the previous section (c.f. Fig. 6). It becomes clear that for short sintered samples as well as for high doping levels there exists a highly conducting grain-boundary phase with a characteristic activation energy of about 0.38 eV. Christie et al. [27] reported an activation energy for grain-boundary conductivity in $Ce_{0.8}$
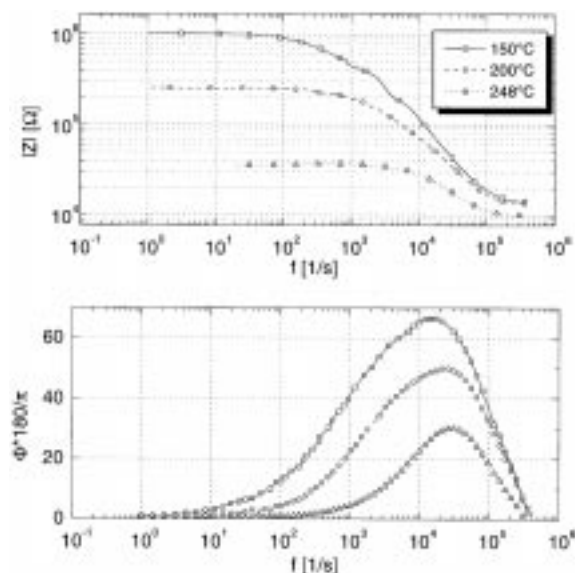
Fig. 11. Bode plots of 1 mol % CoO doped Ce$_{0.8}$Gd$_{0.2}$O$_{2-x}$ sintered for short time (10 min) recorded at different temperatures.

Fig. 13. Bode plots of 1 mol % CoO doped Ce$_{0.8}$Gd$_{0.2}$O$_{2-x}$ sintered for long time (50 h) recorded at different temperatures. Arrows are indicating the characteristic frequency, w_0, of the grain-boundary contribution.

Gd$_{0.2}$O$_{2-x}$ of 0.97–1.17 eV over the temperature range 200–500°C. This is much higher than what we found in our samples. However, the activation energy for σ_e
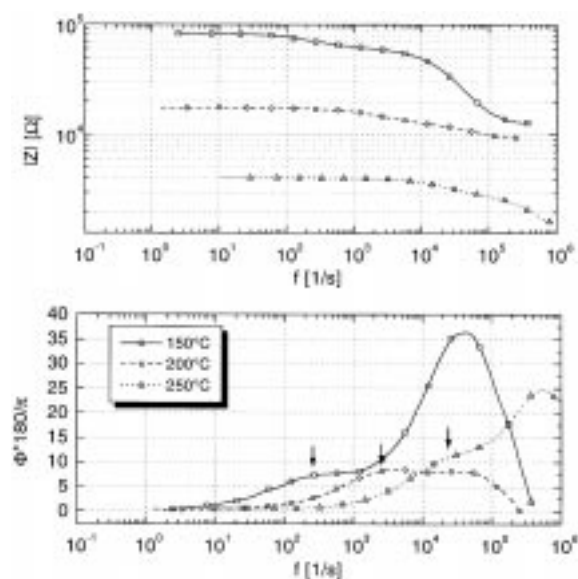
in pure CoO is about 0.25 eV between 100 and 700°C [48] and about 0.54 eV in the range from 900 to 1300°C [49]. We also want to point out the very good

Fig. 12. Bode plots of 1 mol % CoO doped Ce$_{0.8}$Gd$_{0.2}$O$_{2-x}$ sintered for intermediate time (2 h) recorded at different temperatures. Arrows indicate the characteristic frequency, ω_0, of the grain-boundary contribution.
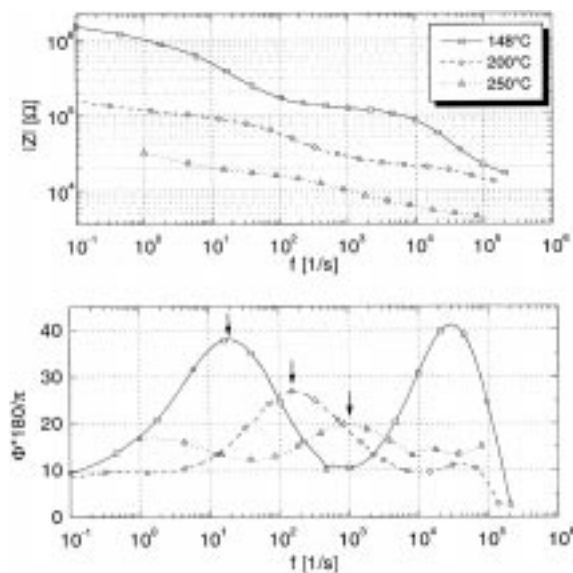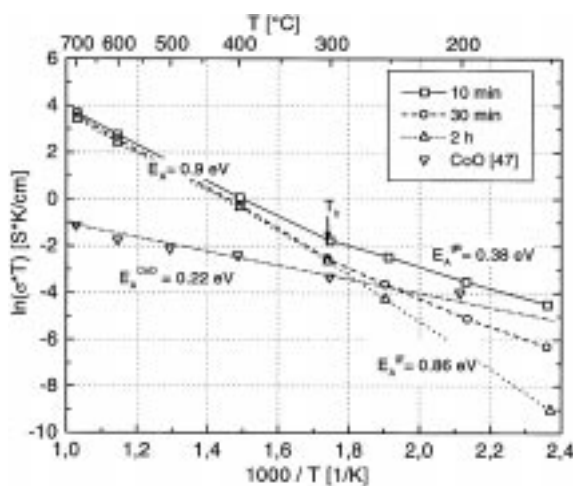

Fig. 14. Arrhenius plot of grain, grain-boundary and total conductivity of Ce$_{0.8}$Gd$_{0.2}$O$_{2-x}$ doped with 1 mol % CoO. The samples were sintered at 900°C for 10 min, 30 min, and 2 h respectively. The slopes, m, of the curves in the $\ln(\sigma_{tot}T)$ versus 1/T were obtained from least-square fits of the experimental data. T_b is the point of intersection where grain-boundary conductivity (dashed lines) equals grain conductivity (dotted line). Conductivity and activation energy of cobalt oxide taken from Beljaev and Studencov [48] is also shown.

agreement of σ_{gb} with σ_e^{CoO} in the temperature range of 150 to 300°C [50].

From these findings we deduce that below 400°C the conductivity is dominated by the about 2 nm thick amorphous cobalt oxide grain boundary layer identified by microstructural analysis (c.f. [19,20]). At temperatures higher than 400°C the ionic conductivity is predominant, T_b (c.f. Fig. 14) indicates the point of intersection, where the grain-boundary conductivity equals the grain contribution. With increasing sintering temperature and time the conductivity changes to lower values with an activation energy of about 0.8 eV corresponding to E_A of pure CGO. Consequently, T_b shifts to lower temperatures. During annealing the cobalt cations from the CoO rich grain boundary layer that first introduced electronic grain boundary conductivity are now incorporated in the CGO lattice. As their concentration is low, this will not give rise to electronic conductivity in the CGO bulk material. On the other hand conductivity of oxygen ions now becomes predominant with clearly separated grain and grain-boundary contributions. Since the conductivity of the long-time sintered sample is now mainly ionic, an electrode response is found also in the low frequency region.

CeO_2 is known to have a high solid solubility for many dopants [51–53]. The cobalt cations are dissolved in the ceria crystal structure during the later stage of sintering. They neither form an ion blocking grain boundary layer nor do they lead to a significant increase in the electronic conductivity of the host material.

The high solubility of cobalt within the CGO lattice observed agrees well with the results of Dontsov et al. who found that the solubility limit of cobalt in the CeO_2 lattice to be 30 mol % at 1600°C

[54]. Also Naumovich et al. reported a solubility limit of cobalt in CGO around 10 mol % [55] after sintering at 1127–1397°C for 50 h. This is in contrast to Sirman et al. who used dynamic SIMS in combination with XRD and determined a solubility limit of about 0.5 mol % after sintering at 1400°C for 50 h [56]. No reaction products between CeO_2 and cobalt oxide in the above mentioned temperature range are reported in the literature.

3.3. Correlation of Conductivity Data with Microstructure

Following the BLM introduced in subsection 2.3 we can now calculate the specific grain-boundary conductivity, σ_{gb}^{sp}, from the data obtained in the impedance spectra (Eq. (8)). The grain-boundary thickness, δ_{gb}, is derived by means of Eq. (2) and Eq. (3). Values for apparent grain sizes are taken from [19]. The results are listed in Table 2 determined from measurements taken at different temperatures, T.

The highest specific grain boundary conductivity (σ_{gb}^{sp}) was found for the 10 min sintered sample, it decreases with longer sintering times. We want to point out that σ_{gb}^{sp} changes more than one order of magnitude (e.g., $8 \cdot 10^{-6}$ to $2.9 \cdot 10^{-7}$ S/m at 200°C) with increasing annealing time whereas the apparent grain size, $\langle D \rangle$, changes only by factor of 1.7. The grain-boundary width calculated for the 10 min sintered sample using the BLM gave an average value of 3.6 nm. This agrees well with microstructural data reported in Kleinlogel and Gauckler [19] where TEM analysis revealed a 2–4 nm thick grain-boundary film being present in short time sintered CGO. The thickness of this grain-boundary film decreases for longer sintering times. The calculated grain-boundary

Table 2. Calculated grain boundary thickness, δ_{gb}, and specific grain boundary conductivity, σ_{gb}^{sp} for 1 mol % CoO doped $Ce_{0.8}Gd_{0.2}O_{2-x}$ samples sintered at 900°C, for times ranging from 10 min to 50 h. The apparent grain-sizes, $\langle D \rangle$, are taken from Kleinlogel and Gauckler [19,20]

Sintering time	T [°C]	$\langle D \rangle$ [nm]	σ_{gb}^{SP} [S/m]	δ_{gb} [nm]
10 min	150	120	$1.2 \cdot 10^{-6}$	4.8
	200		$8 \cdot 10^{-6}$	3.1
	250		$5.2 \cdot 10^{-5}$	2.8
2 h	150	160	$5.4 \cdot 10^{-7}$	0.84
	200		$3 \cdot 10^{-7}$	0.37
	250		$5.5 \cdot 10^{-5}$	0.47
50 h	150	240	$3.2 \cdot 10^{-8}$	0.42
	200		$2.9 \cdot 10^{-7}$	0.31
	250		$1.6 \cdot 10^{-6}$	0.24

thickness from the BLM was 0.56 nm after 2 h and of 0.32 nm after 50 h annealing. This also agrees well with our TEM results which show no indication of a cobalt rich grain-boundary phase after these long-time sintering conditions [19].

Conductivity data of grain-boundaries as a function of grain-size for $Ce_{0.8}Gd_{0.2}O_{1.9}$ have been reported by Christie et al. [27]. They found that σ_{gb}^{sp} for grain sizes exceeding about 1 μm correlates well with the BLM, i.e., little increase of σ_{gb}^{sp} with increasing grain size. For smaller grain sizes in the range of 0.4 to 0.8 μm they found an abnormally high conductivity which they did not attribute to the presence of a grain-boundary phase. A further explanation has not been given by them. Comparing our results with their data we note that σ_{gb}^{sp} of the 10 min sintered material differs only by a factor of 2–3 from their values. σ_{gb}^{sp} of 50 h sintered material agrees very well with the data of Christie, et al. on samples having several μm sized grains.

4. Summary and Conclusions

It was shown in [19,20] that doping of CGO with 1 mol% CoO gives rise to dense ceramic material with grain sizes in the 100 nm range with a several nm thick amorphous cobalt rich grain boundary film when interrupting sintering at 900°C after 10 min. At higher temperatures and/or with increasing annealing time we found that cobalt oxide dissolves in the ceria lattice and the amorphous film vanishes.

We analysed the electrochemical behavior of CGO doped with different concentrations of CoO and sintered under various conditions, and found that in thermally equilibrated material the electrochemical performance in terms of oxygen ion conductivity and electrolytic domain boundary remains unchanged compared to pure CGO.

4-point conductivity data and impedance spectra allowed us to discriminate between different conductivity mechanisms in non equilibrated samples. Electronic conductivity along a percolating cobalt rich grain-boundary layer was found in the short (10 min) sintered material in comparison with oxygen ion conductivity across grains and grain-boundaries in the long-time (50 h) sintered samples. In addition, we were able to calculate the cobalt rich grain boundary layer thickness to be 2–3 nm in 1 mol% CoO doped samples sintered at 900°C for 10 min

with ceria grains of 120 nm in diameter, which is in good agreement with our previously reported TEM results. CoO doped CGO also represents a model system where limitations of the BLM can be demonstrated and analyzed.

Due to the small ceria grain size of < 120 nm in the sintered material we can expect high mechanically stable electrolytes for SOFC applications with improved mechanical properties. In addition, the low sintering temperature of 900–1000°C gives us the opportunity to co-sinter cathode, anode and electrolyte in a single step thereby reducing thermal stresses, chemical reactions of the components and fabrication costs.

CoO doped $Ce_{0.8}Gd_{0.2}O_{2-x}$ ceramics sintered at temperatures as low as 900–1000°C are promising candidates for electrolytes in SOFCs which can be operated at intermediate temperatures with high power output. By choosing the appropriate cobalt oxide concentration and sintering time/temperature we also expect to increase the electrode/electrolyte triple phase boundary length thereby lowering the electrode overpotential.

References

1. N.Q. Minh, *J. Am. Ceram. Soc.*, **76**, 563 (1993).
2. S.A. Barnett, *Energy*, **15**(1), 1 (1990).
3. T. Tsai and S.A. Barnett, *J. Electrochem. Soc.*, **145**(5), 1696 (1998).
4. C. Kleinlogel, M. Godickemeier, K. Honegger, and L.J. Gauckler, in *Ionic and Mixed Conducting Ceramics III*, edited by W.L. Worrell, et al., Pennington, NJ, The Electrochem. Soc. Inc., PV 97-24, 97 (1997).
5. T. Ishihara, H. Matsuda, and Y. Takita, *J. Am. Chem. Soc.*, **116**, 3801 (1994).
6. P. Shuk, H.-D. Wiemhofer, U. Guth, W. Gopel, and M. Greenblatt, *Solid State Ionics*, **89**, 179 (1996).
7. M. Godickemeier and L.J. Gauckler, *J. Electrochem. Soc.*, **145**(2), 414 (1998).
8. T.H. Etsell and S.N. Flengas, *Chem. Rev.*, **70**, 339 (1970).
9. D. Schneider, M. Gödickemeier, and L.J. Gauckler, *J. Electroceramics*, **1:2**, 165 (1997).
10. I. Riess, *Solid State Ionics*, **52**, 127 (1992).
11. I. Riess, M. Gödickemeier, and L.J. Gauckler, *Solid State Ionics*, **90**(1–4), 91 (1996).
12. E. Perry Murray, T. Tsai, and S.A. Barnett, *Nature*, **400**, 649 (1999).
13. P.-L. Chen and I.-W. Chen, *J. Am. Ceram. Soc.*, **76**(6), 1577 (1993).
14. Y.C. Zhou and M.N. Rahaman, *J. Am. Ceram. Soc.*, **78**(4), 981 (1995).
15. J. Van Herle, T. Horita, T. Kawada, N. Sakai, H. Yokokawa, and M. Dokiya, *Solid State Ionics*, **86–88**, 1255 (1996).

16. K. Eguchi, T. Setoguchi, T. Inoue, and H. Arai, *Solid State Ionics*, **52**, 165 (1992).
17. P.-I. Chen and I.-W. Chen, *J. Am. Ceram. Soc.*, **77**(9), 2289 (1994).
18. J. Van Herle, T. Horita, T. Kawada, N. Sakai, H. Yokokawa, and M. Dokiya, *J. Am. Ceram. Soc.*, **80**(4), 933 (1997).
19. C. Kleinlogel and L.J. Gauckler, in *Proceedings SSI-12*, Solid State Ionics, (1999), accepted.
20. C. Kleinlogel and L.J. Gauckler, in *Proceedings SOFC VI*, Honolulu, Hawaii, (1999), accepted.
21. N.M. Beekmans and L. Heyne, *Electrochimica. Acta*, **21**, 303 (1976).
22. T. Van Dijk and A.J. Burgraaf, *Phys. Stat. Sol. (a)*, **63**, 229 (1981).
23. J.E. Bauerl, *J. Phys. Chem. Solids*, **30**, 2657 (1969).
24. J.-H. Hwang, D.S. McLachlan, and T.O. Mason, *J. of Electroceramics*, **3**(1), 7 (1999).
25. N. Bonanos, B.C.H. Steele, and E.P. Butler, in *Impedance Spectroscopy,* edited by J.R. MacDonald (Wiley and Sons, New York, 1988), 191.
26. S.M. Haile, D.L. West, and J. Campbell, *J. Mater. Res.*, **13**(6), 1576 (1998).
27. G.M. Christie and F.P.F. Van berkel, *Solid State Ionics*, **83**, 17 (1996).
28. A.K. Bose and D.P. Ray-Chaudhuri, *Sci. and Culture*, **3**, 246 (1937).
29. M. Godickemeier, B. Heeb, B. Michel, K. Sasaki, P. Bolac, and L.J. Gauchler, *J. of Materials Research*, **9**(5), 1228 (1994).
30. H. Nafe, *Solid State Ionics*, **13**, 255 (1984).
31. T. Kawada, N. Sakai, H. Yokokawa, and M. Dokiya, *Solid State Ionics*, **53–56**, 418 (1992).
32. S.S. Liou and W.L. Worrell, *Appl. Phys.*, **A49**, 25 (1989).
33. E.J.L. Schouler and M. Kleitz, *J. Electrochem. Soc.*, **134**, 1045 (1987).
34. K.R. Thampi, A.J. McEvoy, and J. Van Herle, *J. Electrochem. Soc.*, **142**, 506 (1995).
35. B.C.H. Steele, *Solid State Ionics*, **75**, 157 (1995).
36. P.S. Manning, J.D. Sirman, and J.A. Kilner, *Solid State Ionics*, in press.
37. K. Sasaki, P. Murugaraj, M. Haseidl, and J. Maier, in *Solid Oxide Fuel Cells* V, U. Stimming, S.C. Shingal, H. Tagawa, and W. Lehnert, eds, vol. 97–40, The Electrochem. Soc. Inc., Pennington, NJ, 1190 (1997).
38. H.L. Tuller, in *Nonstoichiometrie in Oxides*, edited by O.T. Sörensen, Academic Press, NY, 271 (1981).
39. R. Korner, M. Ricken, J. Nolting, and I. Riess, *J. Solid State Chem.*, **78**, 136 (1989).
40. M.A. Panhans and R.N. Blumenthal, *Solid State Ionics*, **60**, 279 (1993).
41. M. Mogensen, T. Lindegaard, U.R. Hansen, and G. Mogensen, *J. Electrochem. Soc.*, **141**, 2122 (1994).
42. H.L. Tuller and A.S. Nowick, *J. Electrochem. Soc.*, **126**(2), 209 (1979).
43. M. Godickemeier, *ETH Dissertation No. 11348*, (1996).
44. *The SGTE Substance Database* version 1994, SGTE (Scientific Group Thermodata Europe), Grenoble, France, 1994.
45. T. Kudo and Y. Obayashi, *J. Electrochem. Soc.*, **123**, 415 (1976).
46. T. Kudo and H. Obayashi, *J. Electrochem. Soc.*, **133**(3), 415 (1976).
47. D.L. Maricle, T.E. Swarr, and S. Karavolis, *Solid State Ionics*, **52**, 173 (1992).
48. A.I. Beljaev and J.E. Studencov, *Legkie Metally*, **6**(3), 17 (1937).
49. G. Borchardt, K. Kowalski, J. Nowotny, M. Rekas, and W. Weppner, *J. Eur. Cer. Soc.*, **14**, 369 (1994).
50. C. Wagner and E. Koch, *Z. phys. Chem. B*, **32**, 439 (1936).
51. R.T. Distine, R.N. Blumenthal, and T.F. Kuech, *J. Electrochem. Soc.*, **126**(2), 264 (1979).
52. H. Yahiro, K. Eguchi, and H. Arai, *Solid State Ionics*, **36**, 71 (1989).
53. H. Yahiro, T. Ohuchi, K. Eguchi, and H. Arai, *J. Mater. Sci.*, **23**, 1036 (1988).
54. G. Dontsov, G. Vitter, and C. Déportes, *Rev. Int. Hautes Tempér. et Réfract.*, **9**, 147 (1972).
55. E.N. Naumovic, V.V. Kharton, A.V. Kovalevsky, and V.V. Samokhval, in *Proc. of the 17th Riso International Symposium on Materials Science*, edited by F.W. Poulsen, N. Bonanos, S. Lindevoth, H. Mogensen, B. Zachau-Christiansen, P375 Denmark (1996).
56. J.D. Sirman, D. Waller, and J.A. Kilner, in *Proceedings of the Fith Inl. Symp. on Solida Oxide Fuel Cells*, edited by U. Stimming, S.C. Singhl, H. Tagawa, W. Lehnert. The Electrochemical Society Inc., Pennington, NJ, PV 97-18, 1159 (1997).